Controller Hardware-in-The-Loop Testing of a Multitimescale Control Architecture for Multienergy Systems

Diran Liu, *Graduate Student Member, IEEE*, Edoardo De Din, *Member, IEEE*, Daniele Carta, *Member, IEEE*, and Andrea Benigni, *Senior Member, IEEE*

***Abstract*—To support the transition to a more sustainable energy supply, interest in multienergy systems (MESs) is increasing due to their ability to enhance overall system flexibility and reliability. Within this framework, control approaches play a key role, as they must address the challenges associated with the different dynamics of various energy domains and the balance between loads and the availability of energy resources. Controller hardware-in-the-loop (CHIL) allows for the safe testing of control applications for MESs but it is inevitably challenged by the complexity of those systems. This article presents the CHIL setup designed for MESs. The peculiarities of the setup are described, and its capabilities are evaluated considering a multitimescale control architecture.**

***Index Terms*—Co-simulation, hardware-in-the-loop simulation, multienergy system, voltage control.**

I. Introduction

MULTIENERGY system describes an energy system where different energy carriers, such as electricity, heat, cooling, and fuels interact with each other, coupled through various technologies [1]. In this regard, the progress of these sector-coupling technologies, including heat pump (HP)s, electrolyzers, and fuel cells, has contributed to the recent development of multienergy system (MES). As a result, MES offers numerous advantages over the conventional approach, where each energy sector stays decoupled. For example, it improves the flexibility and reliability of energy systems [1] while enhancing the efficiency [2].

Therefore, electrical grids could benefit from coupling with other energy domains, obtaining flexibility from the other energy sector for demand-response [3], day-ahead scheduling [4], [5], and optimal planning [6]. However, the high penetration of coupling devices into distribution grids, e.g., HPs from the heat grids, introduces new options as well as new challenges for the operation of distribution grids [7], i.e., maintaining the voltage within the operational limits.

Received 28 June 2024; revised 29 December 2024; accepted 23 February 2025. Date of publication 28 February 2025; date of current version 16 April 2025. This work was supported by the European Commission Horizon Europe Programme under Grant 101096511. *(Corresponding author: Edoardo De Din.)*

Diran Liu, Edoardo De Din, and Daniele Carta are with the ICE-1: Energy Systems Engineering, Forschugszentrum Jülich, 52428 Jülich, Germany (e-mail: d.liu@fz-juelich.de; e.de.din@fz-juelich.de; d.carta@fz-juelich.de).

Andrea Benigni is with the RWTH Aachen University, 52056 Aachen, Germany, and also with JARA-Energy, 52425 Jülich, Germany (e-mail: a.benigni@fz-juelich.de).

Digital Object Identifier 10.1109/JESTIE.2025.3546680

In this regard, cooperation between different voltage levels becomes crucial, as the flexibility at the lower voltage level could be used for the higher voltage level for solving congestion and voltage issues [8], [9]. Still, few examples consider the impact of MES in voltage regulation or congestion management of distribution grid [7], [10].

In order to take advantage of the benefits of MES while considering the different dynamics of the energy domains, multitimescale control approaches are often used to control MES. In [11], a multitimescale distributed model predictive control (MPC) for a combined heat and power (CHP)-MES system supplying a university building is proposed, where dedicated MPCs are developed for heat and power systems, each running with a different timescale. Similarly, in [12], the overall MES system is decoupled, according to the different dynamics, into subsystems controlled by dedicated MPCs running at different timescales. In [13], a hierarchical multitimescale MPC control architecture is proposed for an aircraft MES, where the high-level MPC operates on a larger timescale and coordinates with a low-level control with smaller timescale.

The control architectures can be tested under realistic scenarios using a controller hardware-in-the-loop (CHIL) setup, where the controller hardware is interfaced with real-time simulators [14]. In [15], an open-source testbed is introduced, which provides a combination of simulation tools and communication services to support testing and validation using a CHIL setup. The article presents a validation, by means of CHIL, of a coordinated control concept for a heat pump and a coupled power grid. However, the study does not address the coordination between different voltage levels and, consequently, between different controllers. In [16], a novel voltage control for coordinating traditional devices and distributed energy resources in the distribution grid is validated using CHIL. In [17], a CHIL setup is developed for testing the performance of centralized and distributed control architecture, considering communication and different control hardware. Nevertheless, there are few works that test hierarchical control strategies for MES with a CHIL setup. A CHIL test bench is implemented to validate the multitimescale MPC for an aircraft electrical-thermal system in [13], which, however, represents a scenario far from the one considered for this work. In [18], a hierarchical control architecture is proposed to improve the resilience of a community-level MES under emergency conditions, and is validated with a CHIL setup;

yet, the control focuses mainly on the electrical grid, ignoring the control in the thermal domain. Furthermore, these works have not considered multitimescale control architecture.

With regard to the testing of distributed control for distribution grids, only a limited number of studies have considered the use of CHIL in combination with the implementation of the controllers in physical hardware. In [17] and [19], CHIL implementations of distributed control algorithms for distribution grids have been presented, using single-board computer (SBC)s to run the controllers. In [20], the work presented in [19] has been extended to address the multilevel control of distribution grids, whereas in [21] and [22] the extension concerns the development of a flexible container-based architecture. However, it is worth noting that all of these works have exclusively focused on the electrical domain, and that no coordination with controllers dedicated to another energy domain has been tested.

Hence, this article presents a CHIL setup for testing the multitimescale control architecture for MES, in which different hardware is used to implement the components of the control architecture, which are linked to different parts of the MES. Network communication is then employed to interface the controllers with each other and with the MES real-time cosimulation infrastructure. The developed CHIL setup offers the capability of real-time testing, which is essential for the evaluation of distributed control solutions. Although a software-in-the-loop (SIL) setup could have been considered, this would have introduced significant challenges in accurately capturing computational performance and identifying potential bottlenecks. Furthermore, the SIL approach would have posed some limitations in studying the impact of nonideal communication networks and distributed control asynchronous behavior.

With respect to aforementioned works, the present article develops the CHIL setup for testing the multitimescale control for the control of an MES in a scenario where voltage regulation at medium voltage (MV) level is achieved through the flexibility provided by the MES at the low voltage (LV) level while optimizing the operation of the heat grid. Moreover, the deployment of the controllers, in both centralized and distributed configurations, and their coordination within the CHIL setup represents a crucial element of this work.

The contributions of this work are summarized as follows.

1) A CHIL setup is developed to test a proposed multitimescale control architecture, where the different control strategies are implemented on different hardware and the MES is simulated using a cosimulation of heat and electrical domains;
2) A multitimescale control architecture for the MES is proposed, where the coordination between the controllers with different control intervals as well as the coordination between MV and LV levels is addressed;
3) The CHIL setup is employed to evaluate the control architecture in terms of control performance, communication and scalability.

The rest of this article is organized as follows. Section II describes the multivoltage level MES and the hardware-in-the-loop (HIL) lab. Section III describes the proposed multitimescale control architecture. Section IV presents the CHIL setup. Section V reports the results. Finally, Section VI concludes this article.

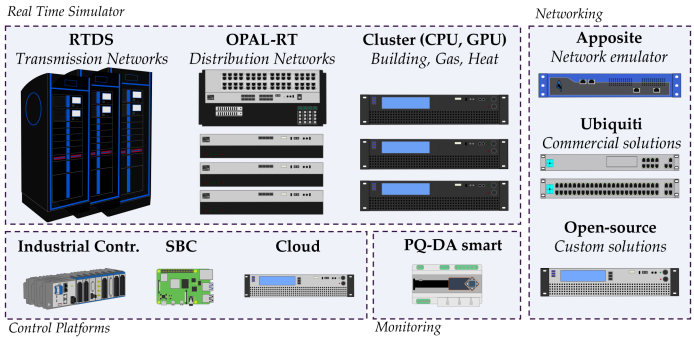

Fig. 1. Overview of the components of the HIL lab.

II. CHIL Approach

The CHIL setup utilized in this work is based on the HIL laboratory developed at Institute of Climate and Energy Research: Energy Systems Engineering (ICE-1) of Forschungszentrum Jülich (FZJ). This HIL lab was designed with two primary objectives: To facilitate the testing of control solutions for energy systems with a comprehensive approach to the involved energy carriers, and to support the testing of control solutions that involve a large number of networked controllers. Fig. 1 shows a simplified diagram of the lab.

The many components of the lab can be grouped according to their function as follows.

1) *Simulation*, both commercial and custom-developed solutions are employed for the simulation of MESs, including power, gas, and heat grids, as well as their interfacing components;
2) *Control*, various control solutions are interfaced with real-time simulators to enable the deployment of newly developed approaches. To accurately represent the diverse requirements of MES control, the lab includes high-performance industrial controllers, single-board computers, and servers for deploying cloud-based architectures;
3) *Networking*, commercial and custom solutions are used to manage communication between simulators (cosimulation), between controllers under test and simulators, and among controllers themselves. To realistically evaluate the impact of nonideal communication in real-world scenarios, network emulators are employed.

The lab infrastructure should then be configured to meet the specific requirements of each considered scenario. A brief overview of the scenario under consideration as a prerequisite to the description of the defined setup is provided as follows.

The multivoltage level MES analyzed in this work, illustrated in Fig. 2, features two voltage LV and MV—and spans two energy domains: electrical (depicted in black) and heat (depicted in red). At the LV level, in addition to a base load, each

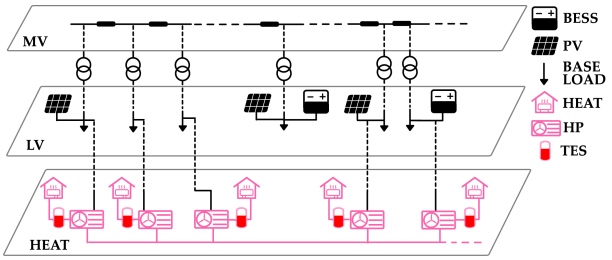

Fig. 2. Simplified graphical representation of the considered multivoltage level MES.

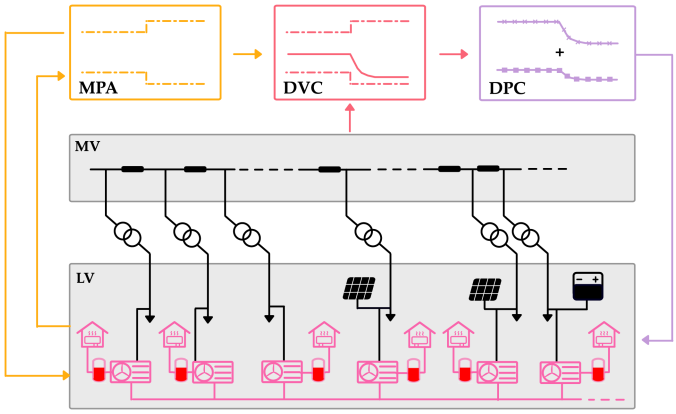

Fig. 3. Coordination of the proposed multitimescale control architecture.

building can be equipped with a HP, thermal energy storage (TES), battery energy storage system (BESS), and photovoltaics (PV). Although HP, TES, BESS, and PV are all controlled in this study, only the flexibility of BESS and PV is utilized for voltage regulation. Each building is connected to the MV level through a MV/LV transformer. The real-time cosimulation is conducted using the setup described in [23] for heat and electrical grid systems, which includes a commercial real-time simulator and a dedicated PC cluster unit for functional mock-up unit (FMU)-based simulation [24]. Each simulation model operates on different simulators at specific time steps, ensuring efficient computation and simulation accuracy. High-performance commercial real-time simulators are primarily used for electrical domain models, which require small time steps to simulate fast dynamics. The HIL lab is equipped with five real-time simulators from OPAL-RT [25], one of which is used in this work for simulating the electrical grid model, while the FMU-based heat grid simulation is deployed on one of the PC cluster units in the HIL lab. Further details are provided in Section IV-A.

The proposed multitimescale control architecture, thoroughly described in Section III, includes both centralized and distributed algorithms, implemented across various hardware components of the HIL lab. Centralized control architectures are typically deployed on dedicated servers or cloud systems [26], so a dedicated server in the HIL lab is used to run the centralized algorithms of the proposed architecture, specifically the maximal-flexibility power aggregation (MPA) and disaggregated power control (DPC). Conversely, the distributed voltage control (DVC), the architecture's distributed algorithm, is implemented using a set of the 100 Raspberry Pi (RPi) units. Implementing distributed control with RPi devices necessitates deploying software components on multiple units. Specifically, the same software runs on all units with different input configurations [27], allowing the use of software containerization to facilitate the execution of replicated packaged software in the RPi cluster [28]. Finally, a central communication gateway has been developed using the open-source software Node-RED [29], serving as the central communication hub for the CHIL setup. In this work, this gateway, running on a dedicated server, manages communications between different simulators and between simulators and controllers. After a detailed description of the proposed MES multitimescale control in Section III, a more comprehensive description of the lab setup will be provided in Section IV.

III. Proposed MES Multitimescale Control

This section presents the multitimescale control architecture that exploits the flexibility of a multivoltage level MES for solving voltage issues in the distribution grid. The architecture is composed of a MPA algorithm to calculate the flexibility at the building level, a DVC to control the voltage of the MV distribution grid, and a DPC algorithm to disaggregate the received cumulative set-points for the flexible resources.

As depicted in Fig. 3, the MPA algorithm calculates for each building connected to the LV grid the available flexibility. The results sent from the MPA to the DVC are the maximal and minimal active and reactive power flexibility that can be requested to be increased or reduced at the MV/LV transformer. The DVC uses the available flexibility as constraints to calculate the set-points for the amount of active/reactive powers that must be increased or reduced at the transformer. Finally, the DPC disaggregates the DVC set-points of active and reactive powers into set-points for each controllable distributed energy resource (DER) device, in this work PV and BESS.

The rest of the section describes in detail each control strategy of the proposed architecture. In Section IV, the proposed architecture is then tested in a CHIL setup.

A. Maximal-Flexibility Power Aggregation

In this work, the MPA algorithm, initially proposed in [30], is used to calculate the maximal flexibility range of both active and reactive power in buildings where DERs are installed. Moreover, the MPA is modified to integrate a MPC, derived from [31], to control the heat grid connecting the HPs while optimizing their power consumption. The MPC controls the heat grid's operation, comprising HPs and TESs, to fulfil the buildings' heat demand, while ensuring compliance with the operational limits of the components over a prediction horizon.

The calculation of the maximal flexibility range is performed by maximizing, over a time horizon, the power flexibility expressed as follows:

$$f_i(t) := w_1|P_i^{\wedge}(t) - P_i^{\vee}(t)| + w_2|Q_i^{\wedge}(t) - Q_i^{\vee}(t)| \quad (1)$$

where $i \in \{1, 2, \ldots, N\}$ represents the MV/LV transformer of the ith node of the MV grid where the individual building is connected and the parameter $t \in \mathcal{T} = \{1, \ldots, T\}$ represents the

MPA iteration, with T the considered time horizon. The variables $P_i^{\wedge}(t)$ and $Q_i^{\wedge}(t) \in \mathbb{R}$ represent the maximum, while $P_i^{\vee}(t)$ and $Q_i^{\vee}(t) \in \mathbb{R}$ represent the minimal active/reactive flexibility power at transformer i, and $w_1 \in \mathbb{R}_+$ and $w_2 \in \mathbb{R}_+$ are the weights for the active and reactive power maximization. In addition, the integrated MPC minimizes, over the time horizon T, the operational costs of the heat grid while fulfilling a set of constraints for the heat grid's operation [31]. These include, among others, the limits on the supplying and return temperature between the pipe network and HPs, limits on the state of charge (SOC) of the TESs and the limits on the supplying temperature from TESs to the buildings.

Since the DVC uses only the result of the first optimization time step t and it does not perform any prediction step instead, an additional objective, from [32], is added to objective (1) to obtain the higher charge/discharge rate of the BESS at the first prediction step and then reduce it over the time horizon. This allows the DVC to exploit the maximal BESS flexibility while relying on the fact that the maximum flexibility calculated by MPA meets the constraints over the whole T. Hence, the objective function is defined as follows:

$$g_i(t) := \left(P_{i,\text{BESS}}^{\vee}(t) + P_{i,\text{BESS}}^{\wedge}(t)\right) \cdot \left(1 - \frac{t-T}{T}\right) \tag{2}$$

where the variables $P_{i,\text{BESS}}^{\wedge}(t)$ and $P_{i,\text{BESS}}^{\vee}(t) \in \mathbb{R}$ represent the maximal and minimal BESS flexible power. Thus, the closer the prediction is to T, the higher the value of $g_i(t)$. Then, minimizing the function corresponds to reducing the BESS power flexibility (and, therefore, the charge/discharge rate). To ensure consistency with the minimization of (2), the maximization of (1) has been reformulated as a minimization problem. Consequently, the overall objective function is formulated as follows:

$$\min \sum_{t=1}^{T} \sum_{i} \left(-f_i(t) + g_i(t)\right) \tag{3}$$

The variables $P_i^{\wedge}(t)$, $Q_i^{\wedge}(t)$ and $P_i^{\vee}(t)$, $Q_i^{\vee}(t)$ are obtained as the sum of the two trajectories, namely, the set of values over a time horizon, calculated for all the flexible components. One represents the maximal active/reactive power (described with $\wedge$ in the superscript), while another represents the minimal active/reactive power (described with $\vee$ in the superscript), resulting, in the active power control as follows:

$$P_i^{\wedge/\vee}(t) = P_{i,\text{load}}(t) + P_{i,\text{BESS}}^{\wedge/\vee}(t) + P_{i,\text{PV}}^{\wedge/\vee}(t) \tag{4}$$

where, $P_{i,\text{load}}(t) \in \mathbb{R}$ represents the sum of the active power consumption of the base load and HP, and $P_{i,\text{PV}}^{\wedge/\vee}(t) \in \mathbb{R}$ the maximal and minimal flexible power for the PV. In this work, only the BESS and PV maximal and minimal trajectories are considered, given that the base load of the buildings and the HPs are treated as nonflexible components. Equivalently, substituting P with Q, the equation for $Q_i^{\wedge/\vee}(t)$ is obtained.

The minimization problem (3) additionally requires a set of constraints, described hereafter.

1) The maximal trajectory must not be smaller than the minimal, meaning that

$$P_i^{\vee}(t) \le P_i^{\wedge}(t), \quad Q_i^{\vee}(t) \le Q_i^{\wedge}(t). \tag{5}$$

2) The operation of PV must fulfill the following constraints:

$$P_{i,\text{PV}}^{\min}(t) \le P_{i,\text{PV}}^{\wedge/\vee}(t) \le P_{i,\text{PV}}^{\max}(t) \tag{6}$$

$$-P_{i,\text{PV}}^{\max}(t)\cos\phi \le Q_{i,\text{PV}}^{\wedge/\vee}(t) \le P_{i,\text{PV}}^{\max}(t)\cos\phi \tag{7}$$

whereas the constraints for the BESS operation are defined as follows:

$$P_{i,\text{BESS}}^{\min} \le P_{i,\text{BESS}}^{\wedge/\vee}(t) \le P_{i,\text{BESS}}^{\max} \tag{8}$$

$$(P_{i,\text{BESS}}^{\wedge/\vee}(t))^2 + (Q_{i,\text{BESS}}^{\wedge/\vee}(t))^2 \le (S_{i,\text{BESS}}^{\text{rated}})^2 \tag{9}$$

$$\text{SOC}_{i,\text{BESS}}(t+1) = \text{SOC}_{i,\text{BESS}}(t) + \frac{\eta_{\text{BESS}} \cdot P_{i,\text{BESS}}(t) \cdot \Delta t}{E_{i,\text{BESS}}} \tag{10}$$

where $P_{i,\text{PV}}^{\max}(t)$ is the maximal available active power of PV at iteration t, whereas $P_{i,\text{BESS}}^{\max}$ and $S_{i,\text{BESS}}^{\text{rated}}$ are the BESS maximal active and apparent power. The parameter $\cos\phi$ is the constant operational power factor of the PV, $SOC_{i,\text{BESS}}$ is the SOC of BESS, $E_{i,\text{BESS}}$ is the BESS capacity, and η_{BESS} is the efficiency of BESS. In this work, the BESS capacity is considered identical for both charging and discharging modes.

3) Using the subscript DER to describe both PV and BESS, the following constraints are defined:

$$P_{i,\text{DER}}^{\vee}(t) \le P_{i,\text{DER}}^{\wedge}(t), \quad Q_{i,\text{DER}}^{\vee}(t) \le Q_{i,\text{DER}}^{\wedge}(t) \tag{11}$$

As proved in [30], if the constraints in (11) are satisfied, each aggregated power within the flexibility range can be always disaggregated into powers for individual controllable DERs that fulfill the constraints in 2).

Together with the result of the optimization, the MPA provides to the DVC the ramping limits for the aggregated power, which are calculated as follows:

$$\Delta P_i^{\text{rated}} = k_{\text{ramp}} \cdot (P_{i,\text{BESS}}^{\text{rated}} + P_{i,\text{PV}}^{\text{rated}}) \tag{12}$$

$$\Delta Q_i^{\text{rated}} = k_{\text{ramp}} \cdot (Q_{i,\text{BESS}}^{\text{rated}} + Q_{i,\text{PV}}^{\text{rated}}) \tag{13}$$

where $\Delta P_i^{\text{rated}}$ and $\Delta Q_i^{\text{rated}}$ are the maximal allowable variable active/reactive power per second, $P_{i,\text{BESS}}^{\text{rated}}$ and $P_{i,\text{PV}}^{\text{rated}}$ the rated active power of BESS and PV, $Q_{i,\text{BESS}}^{\text{rated}}$ and $Q_{i,\text{PV}}^{\text{rated}}$ the rated reactive power, and $k_{\text{ramp}} \in \mathbb{R}$ the ramp rate.

In addition, the MPA provides a variable $\chi(t)$ to DVC, which identifies the priority of using active or reactive power for voltage control.

B. Distributed Voltage Control

The extension of the DVC algorithm to the control of both active and reactive power, presented in [33] and [34] and here briefly described, is divided into two parts: i) dual ascent step of dual variables; ii) minimization of the primal variables. Defining $i \in \mathcal{N}$ a node in the communication graph, with $\mathcal{N} = \{1, 2, \ldots, N\}$ the set of nodes, and $k \in \mathbb{N}$ the iteration of the

algorithm, the dual ascent steps for the active power control results in the following:

$$\lambda_i^{\max}(k+1) = \left[\lambda_i^{\max}(k) + \alpha_i(V_i(k) - V^{\max})\right]_{\geq 0} \quad (14)$$

$$\lambda_i^{\min}(k+1) = \left[\lambda_i^{\min}(k) + \alpha_i(V^{\min} - V_i(k))\right]_{\geq 0} \quad (15)$$

$$\mu_i^{\max}(k+1) = \left[\mu_i^{\max}(k) + \gamma_P(\bar{P}_i(k) - P_i^{\wedge}(t))\right]_{\geq 0} \quad (16)$$

$$\mu_i^{\min}(k+1) = \left[\mu_i^{\min}(k) + \gamma_P(P_i^{\vee}(t) - \bar{P}_i(k))\right]_{\geq 0} \quad (17)$$

where V_i is the measured voltage and $\bar{P}_i(k)$ the primal variable for the active power control calculated at iteration k. Variables $\lambda_i^{\max}$ and $\lambda_i^{\min}$ are the Lagrangian multipliers associated to the voltage ($V^{\max}, V^{\min} \in \mathbb{R}$) constraints, whereas $\mu_i^{\max}$, $\mu_i^{\min}$ are the Lagrangian multipliers associated to the power limits ($P_i^{\wedge}(t), P_i^{\vee}(t) \in \mathbb{R}$) obtained from the MPA, which are constant for all the iterations $k \in \{t-1, t\}$. Moreover, $\alpha_i, \gamma_P \in \mathbb{R}$ are the step sizes for the Lagrangian multipliers update, whereas the $[\cdot]_{\geq 0}$ operator represents the projection into the positive orthant.

For the reactive power control, the dual ascent step follows the same equations presented above, with $\xi_i^{\max}$ and $\xi_i^{\min}$ the Lagrangian multipliers associated with the voltage constraints and $\eta_i^{\max}$ and $\eta_i^{\min}$ the Lagrangian multipliers associated to the power limits ($Q_i^{\wedge}(t), Q_i^{\vee}(t) \in \mathbb{R}$) obtained from the MPA, with step sizes $\beta_i, \gamma_Q \in \mathbb{R}$. Based on the parameter $\chi(t)$ the DVC applies the active or reactive power prioritization by acting on the values of the step sizes α_i and β_i following the method described in [33].

The minimization of the primal variable, for the active power case, follows:

$$\begin{aligned}\bar{P}_i(k+1) = &-(\lambda_i^{\max}(k+1) - \lambda_i^{\min}(k+1)) \\ &- \mathbf{B}_{i,i}(\mu_i^{\max}(k+1) - \mu_i^{\min}(k+1)) \\ &- \sum_{j \in \mathcal{N}_i} \mathbf{B}_{i,j}(\mu_j^{\max}(k+1) - \mu_j^{\min}(k+1)) \quad (18)\end{aligned}$$

where $\mathbf{B}$ is the real part of the admittance matrix and $\mathcal{N}_i$ is the set of neighboring nodes of i. Substituting λ with ξ, μ with η, and $\mathbf{B}$ with $\mathbf{G}$, which is the imaginary part of the admittance matrix, the update of the primal variable $\bar{Q}_i(k+1)$ is obtained.

As described in Section III-A, the MPA also provides the ramp rate limits $\Delta P_i(t)$ and $\Delta Q_i(t)$ for the variation of power at the MV/LV transformer. Hence, such limits are integrated into the DVC with an additional optimization step, which, for the active power control, solves the following:

$$\begin{aligned}\min \quad & \|P_i(k+1) - \bar{P}_i(k+1)\|_2 \\ \text{s.t.} \quad & P_i^{\vee}(t) \leq P_i(k+1) \leq P_i^{\wedge}(t) \\ & |P_i(k+1) - P_i(k)| \leq \Delta P_i(t) \quad (19)\end{aligned}$$

with $P_i(k+1)$ the resulting DVC active power control output for node i. The maximal ramping powers per time step, namely, $\Delta P_i(t)$, is obtained by multiplying $\Delta P_i^{\text{rated}}$ with the iteration time of the DVC. Based on (19), substituting $\bar{P}_i$ with $\bar{Q}_i$, $\{P_i^{\vee}, P_i^{\wedge}\}$ with $\{Q_i^{\vee}, Q_i^{\wedge}\}$ and ΔP_i with ΔQ_i, the reactive power control output Q_i of the DVC is obtained.

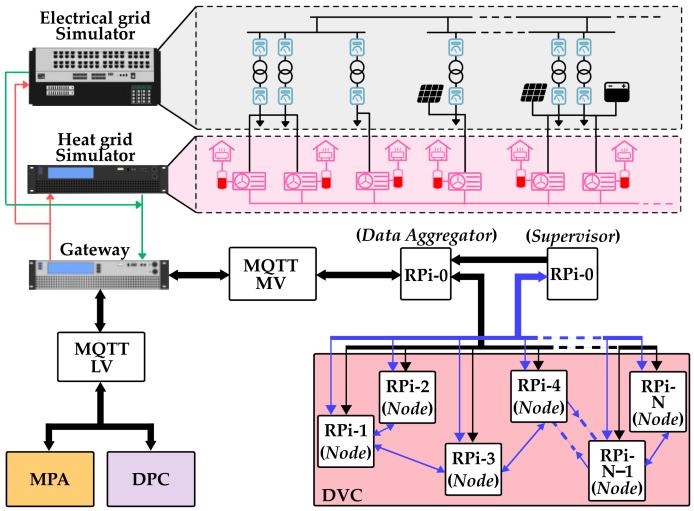

Fig. 4. CHIL setup for MES.

C. Disaggregated Power Control

The DPC is designed to disaggregate the set-points provided by the DVC, which are calculated for each MV/LV transformer, into specific set-points for PVs and BESSs. In the DPC, the active power $P_i(k)$ and reactive power $Q_i(k)$ received from the DVC are disaggregated into a pair of active and reactive power set-points for BESS and PV that fulfill (20) and (21) as follows:

$$P_i(k) = P_{i,\text{PV}}(s) + P_{i,\text{BESS}}(s) \quad (20)$$

$$Q_i(k) = Q_{i,\text{PV}}(s) + Q_{i,\text{BESS}}(s) \quad (21)$$

where s describes the DPC iteration step, whereas $P_{i,\text{BESS}}(s)$, $P_{i,\text{PV}}(s)$, $Q_{i,\text{BESS}}(s)$, and $Q_{i,\text{PV}}(s)$ represent the resulting disaggregated set-points for BESS and PV, respectively, which are obtained based on the ratio between the maximal and minimal flexibility trajectories for BESS and PV.

Finally, the resulting set-points are applied to the simulated BESSs and PVs as described in Section IV.

IV. Development of the CHIL Setup for MES

This section describes the implementation of the CHIL setup, which takes into consideration the control architecture presented in Section III and the HIL lab presented in Section II. This work extends the setup developed in [23] and [35], where a CHIL setup including real-time cosimulation and a gateway for managing communications have been presented. The proposed CHIL implementation is described in Fig. 4, which shows the interactions between the two real-time simulators and between the simulators and the controllers. In the figure, the message queues telemetry transport (MQTT) communication is represented with black arrows, the hypertext transfer protocol (HTTP) with blue arrows, the user datagram protocol (UDP) data received from the simulators, and the UDP data sent to the simulators with green and red arrows, respectively.

A. Cosimulation in the CHIL Setup

As shown in Fig. 4, a real-time heat grid simulator and an electrical grid simulator are coupled over a gateway, which ensures the exchange of data between simulators and thus the realization of the cosimulation. The simulation model for the heat grid is developed in Modelica [36] and exported as a FMU model [24], running on a PC cluster with a time step of 90 s. The electrical grid model is developed in Simulink and runs on an OPAL-RT target with a time step of 200 μs. The time steps are chosen based on the dynamics of heat and electrical systems, given that the dynamics occurring in a heat system are much slower than in the electrical system. The element that couples the two simulation models is the power consumption of HPs: The PC cluster sends results of the power consumption of the HPs to the OPAL-RT target, which integrates this data as load consumption for the electrical grid model.

The workflow of the cosimulation is as follows: at each cosimulation iteration, the OPAL-RT target first sends a request to a communication gateway, which then forwards the request message to the PC cluster. Upon receiving the request message, the PC cluster sends the power consumption results of HPs back to the gateway, which then forwards these results to the OPAL-RT target. Data are exchanged every 90 s and all the communications use UDP protocol.

The customized communication gateway mentioned in Section II is used in the cosimulation. As underlined in Fig. 4 by the red and green arrows, during the cosimulation process, the gateway serves as an intermediary between simulators, for monitoring or visualization purposes.

B. Implementation of Controllers in the CHIL Setup

Both MPA and DPC are implemented in one of the HIL lab servers. The MPA is initialized with the updated measurements from the simulators, such as the SOC of TES, as well as forecasting values such as heat demand predictions. Specifically, the heat grid and electrical grid simulators send the results of the most recent simulation iteration to the MPA before each MPA activation. These variables include all the thermal and electrical simulation data required to solve the MPA, as described in Section III-A. Once the MPA receives the updated data, the optimization model is formulated using COMANDO, which is an open-source Python package for component-oriented modeling and optimization [37]. The resulting optimization model is then solved by means of Gurobi [38], with a maximum optimization time set to 60 s. The optimality gap is calculated as the relative difference between the optimal objective value of the optimization and that of its linear programming relaxation, which represents solution quality [39].

The implementation of the DVC control in the RPi cluster, described in Fig. 5, extends the setup described in [21]. In the proposed setup, the DVC is implemented using Docker containers running on RPi units that serve as the hosting hardware that communicates over a shared network. This is achieved through the use of Swarm mode [40], which facilitates the deployment and orchestration of containers within the RPi cluster. Therefore, a manager node of the swarm is run in one RPi, referred to as RPi-0, while the remaining RPi devices join the swarm as workers. Once the swarm has been created, an overlay network that lays on the physical network is created to connect standalone containers running on different hosts [41]. Finally, the files to deploy the containers are obtained by cloning or pulling updates from a version-controlled online repository, providing consistent code distribution and easy maintenance. These files are as follows: 1) the Dockerfile and Compose, which are the primary files used by Docker to instantiate the container; 2) the algorithm files, which are employed to run the DVC. In the proposed setup, each container, referred to as *Node*, solving the DVC equations for a node $i \in \mathcal{N}$, runs in a RPi and exchanges messages with the other *Node* containers inside an overlay network, as shown in Fig. 5. In addition, RPi-0 is used to run the *Supervisor* container, which provides, via HTTP, the initial information to the *Node* containers, including the portion of matrix $\mathbf{B}$ and $\mathbf{G}$ associated with node i and the set of hostnames of the neighboring RPi units (nodes $j \in \mathcal{N}_i$ in the DVC). To increase the reliability of the proposed approach, the RPi devices are connected to a managed network switch Ubiquiti Switch Pro 48 [42]. This is connected to a Ubiquiti Dream Machine Pro [43], which provides DHCP server functionality, allowing the automatic assignment of IP addresses for the RPi via a web user interface. Thus, if one of the hosts fails, a new RPi can be used to replace the failed one by reassigning the IP address and by cloning the online repository. This high flexibility of the container-based implementation, however, requires provisioning to the container running in each RPi some specific configurations, which can be provided by the user in the form of environmental variables (as . *env* file) via secure shell protocol (SSH), as described by the dashed blue lines in Fig. 5.

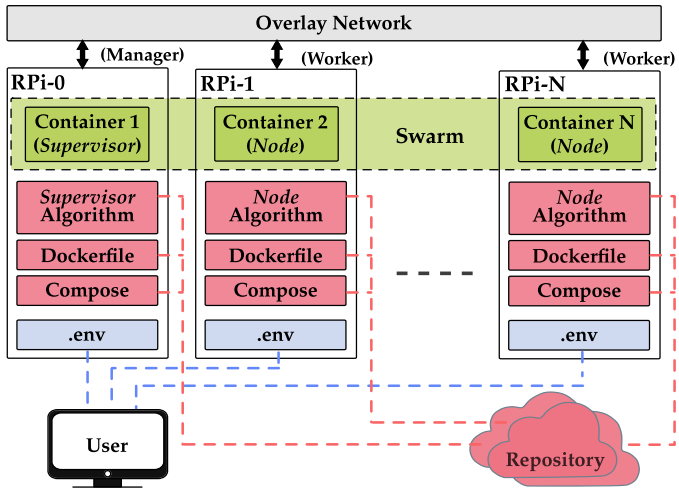

Fig. 5. RPi cluster implementation and interaction with online repository and user.

C. Communication and Timescale Coordination in the CHIL Setup

In the present work, the updating of the control strategies and the data exchange are considered to be coordinated on the

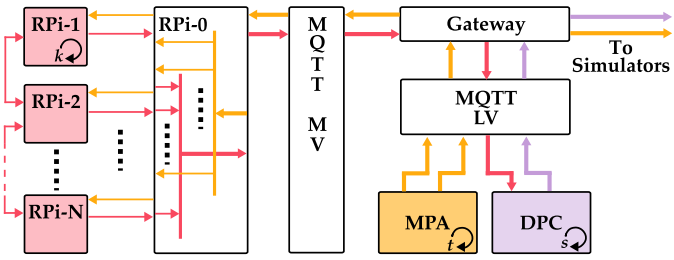

Fig. 6. Coordination and signal exchange of the control architecture.

basis of different timescales. This coordination is necessary, since it allows the execution of the control strategy for different energy domains and, consequently, timescales. As described in Section III-A, the MPA is performed at each iteration t, during which the MPA receives the updated data from the real-time simulators, solves the optimization problem, and sends the flexibility range to the DVC (yellow thick arrow in Fig. 6). In addition, the MPA sends the thermal set-points to control the operation of the heat simulation model (yellow thick arrow to simulators in Fig. 6). In each optimization, the MPA calculates results for the next $T = 10$ time steps, with each time step having an interval of 15 min. The time interval is chosen based on the slow dynamic of the thermal system and based on the reporting rate of the heat demand measurement, also 15 min, which is used by the MPA to calculate the optimal operation of the heat grid. The resulting flexibility range is then sent to both DPC and DVC via the MQTT broker for the LV level (MQTT LV). The selection of the MPA time interval relies on the coordination with both the thermal system and the DVC, given that an erroneous selection of the timescale could have a negative impact on the flexibility calculation for the DVC or on the practical limitations of the control of the thermal system.

At the gateway, the flexibility data are combined with the updated voltage measurements from OPAL-RT and then forwarded to the MQTT broker for the MV level (MQTT MV) every 5 s. The *Data Aggregator* container, running in the RPi-0, subscribes to the MQTT MV to obtain the message (yellow thick arrow in Fig. 6). Consequently, each RPi-i (with $i = \{1, \ldots, 6\}$) selects the message forwarded by RPi-0 according to its hostname (yellow thin arrow in Fig. 6). As described in Section IV-B, each *Node* container running in a RPi from 1 to N starts a new iteration k of the DVC every time a new measurement is received, in this work every 5 s, and communicates via HTTP with the other *Node* containers to calculate the control output (red thin arrow in Fig. 6). Once a *Node* has calculated the control output, the data is sent to the RPi-0 (red thin arrow in Fig. 6).

As depicted in Fig. 4, the *Data Aggregator* container running in the RPi-0 collects, via MQTT, the data from each *Node* based on the set of hostnames of the containers provided by the *Supervisor*, and send the data to the MQTT MV. Since each *Node* container sends the most recent message each time its internal calculation is concluded, the transmission of data to RPi-0 is not synchronized. Therefore, every time a new message is received from RPi 1 to N the RPi-0 updates its data structure and forwards it to the MQTT MV (red thick arrow in Fig. 6).

The gateway forwards, via the MQTT LV, the DVC set-points to the DPC, which performs, at each iteration s every 5 s, the calculation of the disaggregated power references based on the received data and on the flexibility range provided by the MPA. If set-points are missing after a defined maximum waiting time, the missing data are replaced with the most recent ones. Finally, the output of the DPC is sent to the simulators (purple thick arrow in Fig. 6). It is worth mentioning that the gateway used in this work serves the following functionalities: First, it processes the communication messages to the desired format required by the receivers; Second, it forwards messages between the two MQTT brokers and with the simulators.

It is important to highlight that the MQTT does not represent the prevalent standard protocol utilized in distribution grids. However, recent studies have presented novel service-based architectures for managing distribution networks [26], [44]. In this context, the MQTT broker plays a fundamental role in routing the messages to the subscribers based on message topics. Hence, the MQTT broker facilitates the coordination of the messages between the different applications based on the topic names, thereby ensuring full supervision over the routes utilized by each message.

As suggested in [26], an interoperability layer can be used to convert the MQTT messages into the communication protocol required by each device installed in the fields, such as remote terminal unit (RTU)s, sensors and DERs. Software such as VILLASNode [45] or iec104-python [46] can be used to convert MQTT or other protocols into IEC 61850 or IEC 60870-5-104, respectively. For example in [47], VILLASNode has been employed to convert MQTT messages in IEC 61850 GOOSE to communicate with intelligent electronic device (IED)s from different vendors.

Finally, the MQTT broker used in combination with the interoperability layer enhances the capability to collect data from devices that may not be part of the conventional distribution grid infrastructure, i.e., the heat grid. This is discussed in [48] and [49], where protocol converters have been developed to facilitate the data transfer from sensors and actuators installed in smart buildings to the MQTT broker.

V. Results and Discussion

A. System Under Study

The proposed multitimescale control architecture is tested on the IEEE-34-bus feeder, adapted to a three-phase balanced system, where buildings are connected to six selected nodes, as depicted in Fig. 7. In the proposed test scenario, Node 11 and 17 are only equipped with HPs, hence, no flexible power is available on these nodes, while the other four nodes are equipped with HPs, PVs, and BESSs. The heat grid presented in [31], with HPs as coupling technology, is used in this work. The profiles of the heat demand of a typical winter day are used as inputs for heat grid simulation. These profiles have been obtained from measurements of the heat demand of buildings of the FZJ campus and here accordingly adapted. The buildings' electrical load consumption, $P_{i,\text{load}}$ and $Q_{i,\text{load}}$, is considered fixed throughout the simulation, whereas the PV power profiles,

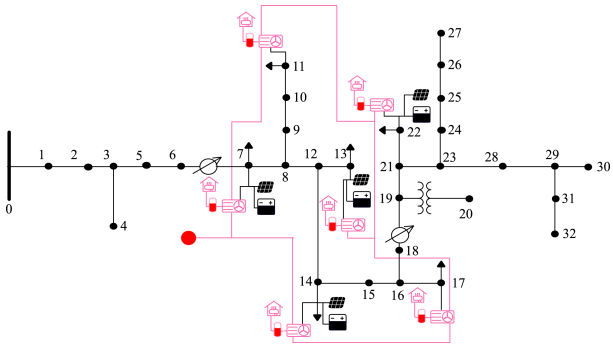

Fig. 7. Schematic overview of the considered network.

TABLE I
NOMINAL PARAMETERS OF BUILDINGS

Node number	$P_{i,\mathrm{PV}}^{\mathrm{rated}}$ [kWp]	$P_{i,\mathrm{BESS}}^{\mathrm{rated}}$ [kW]	$P_{i,\mathrm{load}}$ [kW]	$Q_{i,\mathrm{load}}$ [kvar]	$Q_{i,\mathrm{HP,heat}}$ [$\mathrm{kW_{th}}$]
7	55	80	15	6	60
11	0	0	600	210	700
13	55	80	30	24	200
14	55	80	6	3	60
17	0	0	210	60	700
22	55	80	30	24	200

$P_{i,\mathrm{PV}}^{\max}$, are obtained based on the irradiation data measured at FZJ and on the rated power of PVs. The rated power of PVs, BESSs, electrical load consumption as well as the rated heat output of HPs, namely, $Q_{i,HP,heat}$, have been adapted from the rated values of the FZJ campus. These rated values for the load consumption and for the components connected at each node are summarized in Table I.

The parameters used for the controllers introduced in Section III are summarized as follows: w_1 and w_2 in the objective function (1) are set to 2 and 1, respectively. This gives a higher priority for the active power flexibility calculation. The value of k_{ramp} in (13) is set to 0.01, based on [50]. The value of $S_{i,\mathrm{BESS}}^{\mathrm{rated}}$ is set to be the same as the values of $P_{i,\mathrm{BESS}}^{\mathrm{rated}}$, whereas $E_{i,\mathrm{BESS}}$ of Node 7 and 13 is set to 100 kWh, while $E_{i,\mathrm{BESS}}$ of the other nodes is set to 150 kWh. The efficiency of BESS η_{BESS} is set to 0.9. The constant power factor of PV in (7) is set to 0.9 for all nodes and $Q_{i,\mathrm{PV}}^{\mathrm{rated}}$ in (13) is calculated using $P_{i,\mathrm{PV}}^{\mathrm{rated}}$ and the power factor. The variable $\chi(t)$ is set to give priority to active power, while the values of all the step sizes of DVC are calculated based on [33] and[51].

B. Voltage Control Performance and Coordination Results

The simulation results of Node 17, which is the node with the most noticeable undervoltage, are shown in Fig. 8. The top subplot shows the voltage simulation results, where the dashed line in the subplot is the simulation results of the scenario where the control architecture is not applied, whereas the solid black line represents the voltage resulting from the application of the control. The yellow line shows the voltage limit value $V^{\min}$, equal to 13.66 kV, of the DVC. In the bottom subplot, the solid and dashed lines show the active and reactive power,

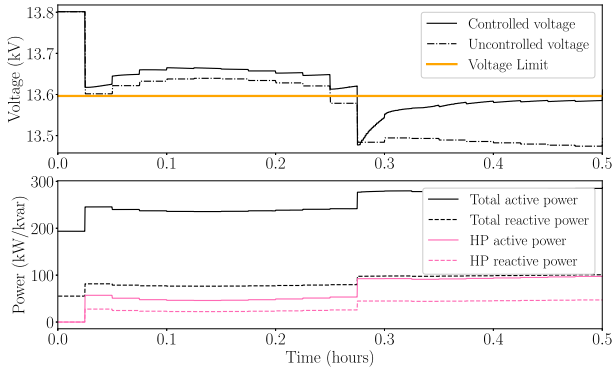

Fig. 8. Cosimulation results, undervoltage recovery for Node 17.

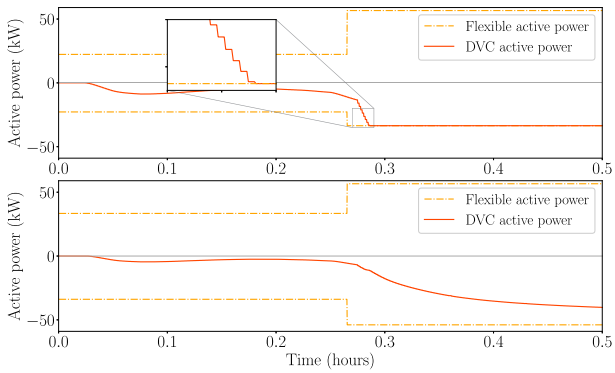

Fig. 9. Active power of the DVC for Node 13 (top) and Node 22 (bottom).

respectively, for the total load at the MV/LV transformer (in black) and for the HP (in pink). The undervoltage, visible near time 0.3 hours, results from the increase of the HPs power at the different nodes (in Fig. 8 shown only for Node 17). This increase is the consequence of the increase of the heat demand in the different buildings, obtained from the heat grid simulation. Hence, the voltage is restored to the minimum limit only when the proposed control is applied.

Fig. 9 shows the result of the DVC control actions at Node 13 and Node 22 to support the undervoltage recovery at Node 11 and 17. In the top subplot, the red line shows the aggregated set-point for the active power of PV and BESS calculated by DVC for Node 13, the yellow dashed lines are the maximal and minimal active power provided, for the same node, by MPA and the gray line indicates the zero point on the y-axis. In this work, the negative values of power indicate the injection of power into the grid. Near the time 0.3 hours, the power injecting into the grid at Node 13 increases significantly and reaches the minimal active power given by MPA, to compensate for the undervoltage observed at around 0.3 hours in Fig. 8. Moreover, the zoomed-in plot shows the iteration steps of the DVC, highlighting the higher rate of the DVC compared with the MPA iteration step.

It is worth noticing that in the second control interval of MPA, the upward flexibility and the downward flexibility are not symmetric. This asymmetry occurs because the discharge of the BESS, to compensate for the undervoltage, results in an

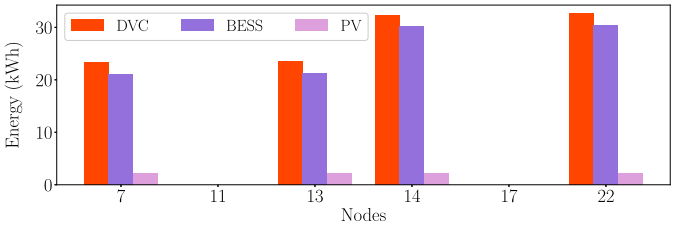

Fig. 10. Energy consumption results of the DVC and the DPC over the simulation period.

TABLE II
COMMUNICATION RESULTS, AVERAGE TRANSMISSION TIME OF PACKETS

Gateway to MQTT MV [s]	MQTT MV to RPi-0 [s]	RPi-6 to RPi-0 [s]	RPi-0 to MQTT MV [s]
4.993 ± 0.001	4.992 ± 0.015	4.935 ± 0.258	4.498 ± 1.323

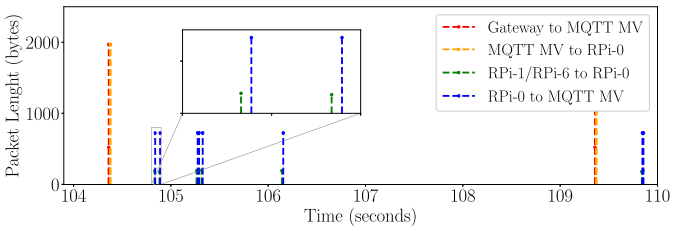

Fig. 11. Results of the communication test in CHIL setup.

insufficient residual SOC to allow for a higher discharging rate. The second subplot shows the active power of DVC results at Node 22. Similar to the results of Node 13, the power injected into the grid significantly increases at around 0.3 hours. Given the prioritization of the active powers in the DVC, the results of the reactive powers, which are zero for the entire simulation time, are not shown for brevity.

Fig. 10 shows the results of DPC, which disaggregates the DVC's result into set-points for PV and BESS. In this plot, the total energy consumption over the simulation period (0.5 hours) is shown for each node where the buildings are connected. The red, dark and light purple pillars represent the energy of DVC set-points, of the BESS and PV resulting set-points, respectively. For each node equipped with BESS and PV, the DVC energy is divided into the energy of BESS and PV. The BESS provides most of the flexible power, given the low PV generation of the simulated scenario.

C. CHIL Setup Communication Results

The coordination of the control architecture in the proposed CHIL setup is tested by monitoring the data exchanged among the components described in Fig. 6. The result of the test is presented in Fig. 11, which shows the packets captured between time 104 s and 110 s of the simulation. In red, the data sent from the gateway to MQTT MV shows a time difference of 5 s between two new packets, thus satisfying the requirements in Section IV-C. The message is immediately forwarded from MQTT MV to the RPi-0 (yellow line). The green line describes the data received by the RPi-0 every time one of the RPi-i (with $i = \{1, \ldots, 6\}$) sends its calculation results. As described in Section IV-C, the RPi-0 adds the last received data from RPi-i to its data structure and sends it to MQTT MV (blue line). Therefore, the length of the packet sent from RPi-0 to MQTT MV is greater than that sent from any RPi-i to RPi-0, since it combines the information received by all RPi-i. The results of the test are summarized in Table II, which shows the calculation of the average time between the transmission of two packets.

The table underlines the high synchronicity of the gateway, as the time difference varies in the order of 0.3%, and, conversely, the asynchronous behavior of the RPi-i (in the table shown for $i = 6$), as their time difference varies up to 26% in transmission of data from RPi-0 to MQTT MV. However, despite the asynchronicity, the proposed architecture is capable of providing control set-points, under the HIL lab network conditions, within 5 s.

D. CHIL Scalability Results

The scalability of the control architecture with respect to the increase of the problem size is evaluated in terms of the time required for the most time-critical components of the setup to execute their algorithms. To perform the tests, the same grid described in Section V-A has been utilized, with 12, 18, and 24 buildings randomly positioned within the grid and with the parameters randomly selected from Table I.

The tests performed are the following: 1) The optimality gap when the maximum optimization time is reached by the MPA to perform the optimization problem; 2) Time required by RPi-N, with N the largest node number, to send the message to RPi-0.

1) MPA Scalability: The scalability tests of MPA utilize the identical constraints and optimization objective as defined in Section III-A, with the number of buildings included in the MPA increasing while other settings remain constant. For each set of nodes, the optimality gap achieved by each optimization conducted by the MPA during a total simulation scenario of four hours is recorded. Subsequently, the mean optimality gap with the associated standard deviation is calculated for the entire simulation duration, as described in Table III. To perform such tests, the FMU model of the heat grid and the distribution grid models performed in OPAL-RT are adjusted accordingly.

As the size of the problem increases, it becomes more challenging for the MPA to identify feasible solutions within the maximum optimization time of 60 s. However, this represents a crucial aspect to ensure real-time operation of the entire setup [52]. Despite these challenges, the results in Table III show that feasible solutions with acceptable optimality gaps remain achievable even when the number of buildings increases by a factor of four. In particular, the optimality gap rises from 4.637% to 8.785% , thus remaining below 10% . This demonstrates that the optimality gap remains acceptable with the increasing size of the problem.

2) DVC Scalability: The tests employ the same methodology utilized in Section V-C, but focus specifically on the time interval between data reception from the RPi-N device on RPi-0. The tests have been performed by collecting

TABLE III
RESULTS OF THE SCALABILITY

Number of nodes	MPA optimality gap [%]	RPi-N RPi-0 [s]
6	4.637 ± 3.261	4.935 ± 0.258
12	7.077 ± 0.853	4.875 ± 0.269
18	7.747 ± 0.791	5.080 ± 0.338
24	8.785 ± 0.287	5.021 ± 0.266

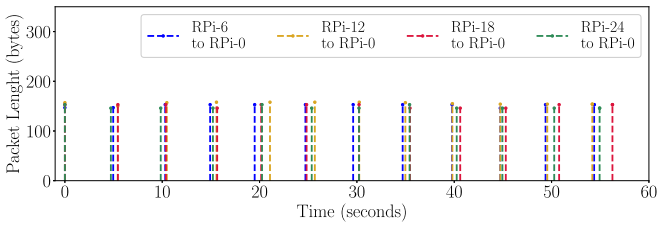

Fig. 12. Results of the DVC scalability test.

the MQTT messages sent by RPi-N to RPi-0 over 10 min. The results of the DVC scalability tests are presented in Fig. 12 and in Table III. The figure presents a 1-min interval of the packets captured during the test, with the number of nodes increasing incrementally, where, to facilitate the comparison, the initial samples within the selected time window have been aligned. The comparison of the packets from the different cases reveals that the packets are approximately aligned around 5-s intervals.

Moreover, the table shows in the column named RPi-N to RPi-0 that the average time intervals remain relatively constant as the total number of nodes increases. The results demonstrate that increasing the number of nodes of the DVC does not affect its scalability, given that each control node i in the RPi performs its calculation autonomously, communicating only with a small set of neighbors. These findings confirm those presented in [21], which were conducted exclusively within Docker containers. As a result, each control node i is capable of calculating the control output in a relatively short time period, thereby allowing the *Data Aggregator* to collect data from all the nodes within the specified time window, thus ensuring the real-time performance of the setup.

It is worth noting that the simultaneous activation of a significant number of nodes in DVC, that is, the involvement of several control nodes in the voltage regulation on the basis of local measurements or data exchange with neighboring nodes, is not a realistic scenario, given the inherent local nature of the voltage control problem.

Therefore, since the voltage issue is a localized event within the grid, although all the N nodes of the DVC send the data to the *Data Aggregator*, only a subset of them are actually involved in solving the voltage problem, while the remaining nodes send null values.

VI. CONCLUSION

This work presents a CHIL setup for testing a multitimescale control architecture for a multivoltage level MES, in which an electrical grid is coupled with a heat grid. Through the testing of the control architecture, two aspects of the complexity of an MES at the distribution level are addressed: dynamics of each energy domain and cooperation between voltage levels in the electric grid. The CHIL setup comprises real-time simulators for the cosimulation of electrical and heat grids, cloud and RPi-based controllers, and communication infrastructure to interface controllers and simulators.

The proposed multitimescale control features MPA for the definition of flexibility at the LV level, DVC for the calculation of active and reactive power set-points at the point of connection with the MV level, DPC that disaggregates the DVC set-points into reference values for the flexible resources.

The results of the CHIL testing show that the multitimescale control can effectively handle different dynamics of multienergy domains while ensuring direct cooperation across different voltage levels in the electrical grid. The results also show the DVC at MV is capable of restoring the undervoltage, caused by the increase of the HP power consumption, using the flexibility range provided by MPA.

In addition, the tests demonstrate the benefits of CHIL testing of the control architecture, encompassing different control platforms and communication protocols, in a safe but realistic environment. The tests highlight how the implementation of such multitimescale control architecture on physical hardware introduces realistic behavior, e.g., asynchronous mode of the DVC, which, thanks to the CHIL setup, can be examined. Furthermore, the tests have demonstrated the high flexibility of the proposed setup, which allows for a gradual increase in the size of the control problem while ensuring high scalability.

Indications of future developments from this work are several: 1) The control architecture could be extended for applications that include coordination with flexible resources at MV level and considerations of additional flexible devices on LV, such as electrical vehicle (EV)s; 2) the CHIL setup could be extended with real-time simulation of additional energy domain, e.g., gas, and with new control strategies and platforms; 3) the CHIL setup could be extended with the network emulation to mimic different network conditions.

ACKNOWLEDGMENT

Views and opinions expressed are, however, those of the author(s) only and do not necessarily reflect those of the European Union or CINEA. Neither the European Union nor the granting authority can be held responsible for them.

REFERENCES

[1] P. Mancarella, "MES (multi-energy systems): An overview of concepts and evaluation models," *Energy*, vol. 65, pp. 1–17, 2014.
[2] Y.-G. Son, B.-C. Oh, M. A. Acquah, R. Fan, D.-M. Kim, and S.-Y. Kim, "Multi energy system with an associated energy hub: A review," *IEEE Access*, vol. 9, pp. 127753–127766, 2021.
[3] N. Good and P. Mancarella, "Flexibility in multi-energy communities with electrical and thermal storage: A stochastic, robust approach for multi-service demand response," *IEEE Trans. Smart Grid*, vol. 10, no. 1, pp. 503–513, Jan. 2019.
[4] D. Xu, Q. Wu, B. Zhou, C. Li, L. Bai, and S. Huang, "Distributed multi-energy operation of coupled electricity, heating, and natural gas networks," *IEEE Trans. Sustain. Energy*, vol. 11, no. 4, pp. 2457–2469, Oct. 2020.

[5] H. Xiao, F. Long, L. Zeng, W. Zhao, J. Wang, and Y. Li, "Optimal scheduling of regional integrated energy system considering multiple uncertainties and integrated demand response," *Electric Power Syst. Res.*, vol. 217, 2023, Art. no. 109169.

[6] W. Huang, N. Zhang, J. Yang, Y. Wang, and C. Kang, "Optimal configuration planning of multi-energy systems considering distributed renewable energy," *IEEE Trans. Smart Grid*, vol. 10, no. 2, pp. 1452–1464, Mar. 2019.

[7] P. Zhao et al., "Economic-effective multi-energy management considering voltage regulation networked with energy hubs," *IEEE Trans. Power Syst.*, vol. 36, no. 3, pp. 2503–2515, May 2021.

[8] A. Kulmala et al., "Hierarchical and distributed control concept for distribution network congestion management," *IET Gener., Transmiss. Distrib.*, vol. 11, no. 3, pp. 665–675, 2017.

[9] A. Baviskar, K. Das, M. Koivisto, and A. D. Hansen, "Multi-voltage level active distribution network with large share of weather-dependent generation," *IEEE Trans. Power Syst.*, vol. 37, no. 6, pp. 4874–4884, Nov. 2022.

[10] P. Yu, C. Wan, Y. Song, and Y. Jiang, "Distributed control of multi-energy storage systems for voltage regulation in distribution networks: A back-and-forth communication framework," *IEEE Trans. Smart Grid*, vol. 12, no. 3, pp. 1964–1977, May 2021.

[11] Y. Jin, X. Wu, and J. Shen, "Power-heat coordinated control of multiple energy system for off-grid energy supply using multi-timescale distributed predictive control," *Energy*, vol. 254, 2022, Art. no. 124336.

[12] L. Wu, X. Yin, L. Pan, and J. Liu, "Distributed economic predictive control of integrated energy systems for enhanced synergy and grid response: A decomposition and cooperation strategy," *Appl. Energy*, vol. 349, 2023, Art. no. 121627.

[13] J. P. Koeln, H. C. Pangborn, M. A. Williams, M. L. Kawamura, and A. G. Alleyne, "Hierarchical control of aircraft electro-thermal systems," *IEEE Trans. Control Syst. Technol.*, vol. 28, no. 4, pp. 1218–1232, Jul. 2020.

[14] A. Benigni, T. Strasser, G. D. Carne, M. Liserre, M. Cupelli, and A. Monti, "Real-time simulation-based testing of modern energy systems: A review and discussion," *IEEE Ind. Electron. Mag.*, vol. 14, no. 2, pp. 28–39, Jun. 2020.

[15] E. Widl, A. Sporr, R.-R. Schmidt, T. Natiesta, and N. Marx, "DigitalEnergyTestbed: An open testbed prototype for integrated energy systems," in *Proc. Open Source Modelling Simul. Energy Syst.*, 2023, pp. 1–7.

[16] A. Newaz, J. Ospina, and M. O. Faruque, "Controller hardware-in-the-loop validation of coordinated voltage control scheme for distribution systems containing inverter-based distributed generation," *IEEE J. Emerg. Sel. Topics Ind. Electron.*, vol. 3, no. 2, pp. 332–341, Apr. 2022.

[17] S. Nigam, O. Ajala, and A. D. Dominguez-Garcia, "A controller hardware-in-the-loop testbed: Verification and validation of microgrid control architectures," *IEEE Electrific. Mag.*, vol. 8, no. 3, pp. 92–100, Sep. 2020.

[18] M. Chamana et al., "Buildings participation in resilience enhancement of community microgrids: Synergy between microgrid and building management systems," *IEEE Access*, vol. 10, pp. 100922–100938, 2022.

[19] Y. Wang, T. L. Nguyen, Y. Xu, Z. Li, Q.-T. Tran, and R. Caire, "Cyber-physical design and implementation of distributed event-triggered secondary control in islanded microgrids," *IEEE Trans. Ind. Appl.*, vol. 55, no. 6, pp. 5631–5642, Nov./Dec. 2019.

[20] Y. Wang, T.-L. Nguyen, Y. Xu, Q.-T. Tran, and R. Caire, "Peer-to-peer control for networked microgrids: Multi-layer and multi-agent architecture design," *IEEE Trans. Smart Grid*, vol. 11, no. 6, pp. 4688–4699, Nov. 2020.

[21] E. D. Din, M. Pitz, F. Ponci, and A. Monti, "Implementation of the online distributed voltage control based on containers," in *Proc. Int. Conf. Smart Energy Syst. Technol.*, 2022, pp. 1–6.

[22] T. L. Nguyen, A. Alrashide, and O. Mohammed, "A cyber-physical platform to assess power system operation with communication network and heterogeneous controllers," *IEEE Trans. Ind. Appl.*, vol. 60, no. 3, pp. 4776–4785, May/Jun. 2024.

[23] D. Liu, D. Hering, D. Carta, A. Xhonneux, D. Müller, and A. Benigni, "A hardware-in-the-loop co-simulation of multi-modal energy system for control validation," in *Proc. 47th Ann. Conf. IEEE Ind. Electron. Soc.*, 2021, pp. 1–6.

[24] "Functional Mock-up Interface." Accessed: Mar. 11, 2025. [Online]. Available: https://fmi-standard.org/

[25] "OPAL-RT." Accessed: Mar. 11, 2025. [Online]. Available: https://www.opal-rt.com/

[26] M. Pau, M. Mirz, J. Dinkelbach, P. Mckeever, F. Ponci, and A. Monti, "A service oriented architecture for the digitalization and automation of distribution grids," *IEEE Access*, vol. 10, pp. 37050–37063, 2022.

[27] S. Rath, D. Pal, P. S. Sharma, and B. K. Panigrahi, "A cyber-secure distributed control architecture for autonomous AC microgrid," *IEEE Syst. J.*, vol. 15, no. 3, pp. 3324–3335, Sep. 2021.

[28] R. Mahmud and A. N. Toosi, "Con-Pi: A distributed container-based edge and fog computing framework," *IEEE Internet Things J.*, vol. 9, no. 6, pp. 4125–4138, Mar. 2022.

[29] "Node-RED." Accessed: Mar. 11, 2025. [Online]. Available: https://nodered.org/

[30] X. Chen, E. Dall'Anese, C. Zhao, and N. Li, "Aggregate power flexibility in unbalanced distribution systems," *IEEE Trans. Smart Grid*, vol. 11, no. 1, pp. 258–269, Jan. 2020.

[31] D. Hering, M. E. Cansev, E. Tamassia, A. Xhonneux, and D. Müller, "Temperature control of a low-temperature district heating network with model predictive control and mixed-integer quadratically constrained programming," *Energy*, vol. 224, 2021, Art. no. 120140.

[32] B. v. d. Holst et al., "A quantification method for the potential downward flexibility of full-electric heat pumps during congestion events," in *Proc. IEEE Belgrade PowerTech*, 2023, pp. 1–6.

[33] E. D. Din, M. Pau, F. Ponci, and A. Monti, "A coordinated voltage control for overvoltage mitigation in lv distribution grids," *Energies*, vol. 13, no. 8, 2020, Art. no. 2007.

[34] N. Patari, A.K. Srivastava, G. Qu, and N. Li, "Distributed voltage control for three-phase unbalanced distribution systems with DERs and practical constraints," *IEEE Trans. Ind. Appl.*, vol. 57, no. 6, pp. 6622–6633, Nov./Dec. 2021.

[35] D. Liu, D. Carta, A. Xhonneux, D. Müller, and A. Benigni, "An MQTT gateway for HIL testing of energy systems," in *Proc. 48th Annu. Conf. IEEE Ind. Electron. Soc.*, 2022, pp. 1–6.

[36] "Modelica." Accessed: Mar. 11, 2025. [Online]. Available: https://modelica.org/

[37] M. Langiu et al., "COMANDO: A next-generation open-source framework for energy systems optimization," *Comput. Chem. Eng.*, vol. 152, 2021, Art. no. 107366.

[38] "Gurobi optimization," *Gurobi*. Accessed: Mar. 11, 2025. [Online]. Available: https://www.gurobi.com/

[39] R. M. Alfant, T. Ajayi, and A. J. Schaefer, "Evaluating mixed-integer programming models over multiple right-hand sides," *Operations Res. Lett.*, vol. 51, no. 4, pp. 414–420, 2023. [Online]. Available: https://www.sciencedirect.com/science/article/pii/S0167637723000688

[40] "Swarm mode key concepts." Accessed: Mar. 11, 2025. [Online]. Available: https://docs.docker.com/engine/swarm/key-concepts/

[41] "Overlay network driver." Accessed: Mar. 11, 2025. [Online]. Available: https://docs.docker.com/network/drivers/overlay/

[42] "Ubiquiti Switch Pro 48." Accessed: Mar. 11, 2025. [Online]. Available: https://techspecs.ui.com/unifi/switching/usw-pro-48

[43] "Ubiquiti Dream Machine Pro." Accessed: Mar. 11, 2025. [Online]. Available: https://techspecs.ui.com/unifi/unifi-cloud-gateways/udm-pro

[44] P. Kannisto, A. Supponen, S. Repo, and D. Hästbacka, "Electricity system built on cyber-physical enterprises: Architecture analysis," *IFAC-PapersOnLine*, vol. 56, no. 2, pp. 8197–8202, 2023.

[45] "VILLASNode." Accessed: Mar. 11, 2025. [Online]. Available: https://villas.fein-aachen.org/docs/node/

[46] "iec104-python." Accessed: Mar. 11, 2025. [Online]. Available: https://iec104-python.readthedocs.io/latest/

[47] T. Penthong, A. Dognini, E. D. Din, M. Pitz, F. Ponci, and A. Monti, "Hardware-in-the-loop validation of AC/DC service restoration including industrial IED and communication protocols," in *Proc. Open Source Modelling Simul. Energy Syst.*, 2024, pp. 1–6.

[48] P. Martins, S. I. Lopes, and A. Curado, "Designing a FIWARE-based smart campus with IoT edge-enabled intelligence," in *Trends and Applications in Information Systems and Technologies*, Á. Rocha, H. Adeli, G. Dzemyda, F. Moreira, and A. M. Ramalho Correia, Eds. Cham, Switzerland: Springer Int. Publishing, 2021, pp. 557–569.

[49] L. Westphal, M. Schröder, D. Carta, A. Xhonneux, A. Benigni, and D. Müller, "Development and application of a FIWARE-based ICT-Platform for multi-energy systems on building and district level," in *Proc. Open Source Modelling Simul. Energy Syst.*, 2024, pp. 1–6.

[50] L. Wang, F. Bai, R. Yan, and T. K. Saha, "Real-time coordinated voltage control of PV inverters and energy storage for weak networks with high PV penetration," *IEEE Trans. Power Syst.*, vol. 33, no. 3, pp. 3383–3395, May 2018.

[51] S. Bolognani, R. Carli, G. Cavraro, and S. Zampieri, "On the need for communication for voltage regulation of power distribution grids," *IEEE Trans. Control Netw. Syst.*, vol. 6, no. 3, pp. 1111–1123, Sep. 2019.

[52] L. Wu and R. D. Braatz, "A direct optimization algorithm for input-constrained MPC," *IEEE Trans. Autom. Control*, vol. 70, no. 2, pp. 1366–1373, Feb. 2025.

Diran Liu (Graduate Student Member, IEEE) received the B.Sc. degree in energy and environment system engineering from Shandong University, Jinan, China, in 2017, and the M.Sc. degree in energy science and engineering from the Technical University of Darmstadt, Darmstadt, Germany in 2020. She is currently working toward the Ph.D. degree in mechanical engineering with the "Institute of Energy and Climate Research: Energy Systems Engineering (ICE-1)," Forschungszentrum Jülich, Jülich, Germany.

Edoardo De Din (Member, IEEE) received the B.Sc. and M.Sc. degrees in electrical engineering from the University of Trieste, Trieste, Italy, in 2013 and 2015, respectively, and the Ph.D. degree in electrical engineering from RWTH-Aachen University, Aachen, Germany, in 2023.

Currently, he is with the "Control Solution" group, "Institute of Energy and Climate Research: Energy Systems Engineering (ICE-1)," Forschungszentrum Jülich, Jülich, Germany.

Daniele Carta (Member, IEEE) received the B.Sc. and M.Sc. degrees in electrical engineering and the Ph.D. degree from the University of Cagliari, Cagliari, Italy, in 2013, 2016, and 2020, respectively.

Currently, he is the Department Leader with the "Control Solution" group, "Institute of Energy and Climate Research: Energy Systems Engineering (ICE-1)," Forschungszentrum Jülich, Jülich, Germany.

Andrea Benigni (Senior Member, IEEE) received the B.Sc. and M.Sc. degrees in electrical engineering from Politecnico di Milano, Milano, Italy, in 2005 and 2008, respectively, and the Ph.D. degree in electrical engineering from RWTH-Aachen University, Aachen, Germany, in 2013.

From 2014 to 2019, he was an Assistant Professor with the Department of Electrical Engineering, University of South Carolina, Columbia, SC, USA. Since 2019, he has been a Full Professor with RWTH-Aachen and the Director of the "Institute of Energy and Climate Research: Energy Systems Engineering (ICE-1)" with the Forschungszentrum Jülich, Jülich, Germany.